Continental Shelf Research 66 (2013) 92–104

Contents lists available at ScienceDirect

Continental Shelf Research

journal homepage: www.elsevier.com/locate/csr

Research papers

The genesis of sea level variability in the Barents Sea

Denis L. Volkov [a,*], Felix W. Landerer [b], Sergey A. Kirillov [c,d]

[a] Cooperative Institute for Marine and Atmospheric Studies, University of Miami, and Atlantic Oceanographic and Meteorological Laboratory, NOAA, Miami, FL, USA,
[b] Jet Propulsion Laboratory, California Institute of Technology, Pasadena, CA, USA
[c] Arctic and Antarctic Research Institute, Saint-Petersburg, Russia
[d] Department of Oceanology, St. Petersburg State University, St. Petersburg, Russia

ARTICLE INFO

Article history:
Received 11 March 2013
Received in revised form
4 July 2013
Accepted 16 July 2013
Available online 27 July 2013

Keywords:
Barents Sea
Sea level variability
Satellite altimetry
GRACE
ECCO2
Arctic seas

ABSTRACT

The regional variability of sea level is an integral indicator of changing oceanographic conditions due to different processes of oceanic, atmospheric, and terrestrial origin. The present study explores the nature of sea level variability in the Barents Sea—a marginal shelf sea of the Arctic Ocean. A characteristic feature that distinguishes this sea from other Arctic shelf seas is that it is largely ice free throughout the year. This allows continuous monitoring of sea level by space-borne altimeters. In this work we combine satellite altimetry, ocean gravity measurements by GRACE satellites, available hydrography data, and a high-resolution ocean data synthesis product to estimate the steric and mass-related components of sea level in the Barents Sea. We present one of the first observational evidence of the local importance of the mass-related sea level changes. The observed 1–3 month phase lag between the annual cycles of sea level in the Barents Sea and in the Nordic seas (Norwegian, Iceland, Greenland seas) is explained by the annual mass-related changes. The analysis of the barotropic vorticity budget shows that the mass-related sea level variability in the central part of the Barents Sea is determined by the combined effect of wind stress, flow over the varying bottom topography, and dissipation, while the impact of vorticity fluxes is negligible. Overall, the steric sea level has smaller amplitudes and mainly varies on the seasonal time scale. The thermosteric sea level is the main contributor to the steric sea level along the pathways of the Atlantic inflow into the Barents Sea. The relative contribution of the halosteric sea level is dominant in the southeastern, eastern, and northern parts of the Barents Sea, modulated by the seasonal sea ice formation/melt as well as by continental runoff. The variability of the thermosteric sea level in the Barents Sea is mostly driven by variations in the net surface heat flux, whereas the contribution of heat advection becomes as important as the ocean-atmosphere heat exchange at interannual time scales.

1. Introduction

The Barents Sea (BS) is a marginal sea of the Arctic Ocean located on the continental shelf between the northern European coast and three archipelagoes—Spitsbergen, Franz Josef Land, and Novaya Zemlya (Fig. 1a). It is a rather deep shelf sea with an average depth of 222 m and a maximum depth of about 600 m. The river runoff is small (163 km^3/year) compared to other marginal seas of the Arctic Ocean; the Pechora River contributes most of the runoff (130 km^3/year) [Lebedev et al., 2011]. The atmospheric circulation over the BS is dominated by cyclones coming from the North Atlantic. The strongest atmospheric pressure gradients are observed in winter months, when southwesterly and westerly winds prevail in the southern part of the sea and southeasterly and easterly winds dominate in the north (Terziev et al., 1990).

The BS is one of the gateways between the Atlantic and the Arctic oceans (Fig. 1a). Approaching the southwestern boundary of the BS the Norwegian Atlantic Current (NwAC) splits into the West Spitsbergen Current that flows north towards the Fram Strait, and into the North Cape Current that veers eastward and enters the BS between the continent and Bear Island. The NwAC transports warm and salty Atlantic Water (AW), about half of which enters the BS (Skagseth et al., 2008). The Norwegian Coastal Current enters the BS along the coastline and also carries some AW. While transiting the BS, the AW undergoes transformation due to heat loss to the atmosphere, mixing with ambient water masses, net precipitation, river runoff, and ice freezing and melting. Substantially modified water then exits the BS primarily to the north of Novaya Zemlya (Loeng et al., 1993). Changes in the volume and properties of the AW inflow as well as changes in atmospheric circulation and buoyancy fluxes greatly impact the variability of

* Corresponding author. Atlantic Oceanographic and Meteorological Laboratory, NOAA/PhOD, 4301 Rickenbacker Causeway, Miami, FL 33149, USA. Tel.: +1 305 361 4344.
E-mail address: Denis.Volkov@noaa.gov (D.L. Volkov).

0278-4343/$ - see front matter © 2013 Elsevier Ltd. All rights reserved.
http://dx.doi.org/10.1016/j.csr.2013.07.007

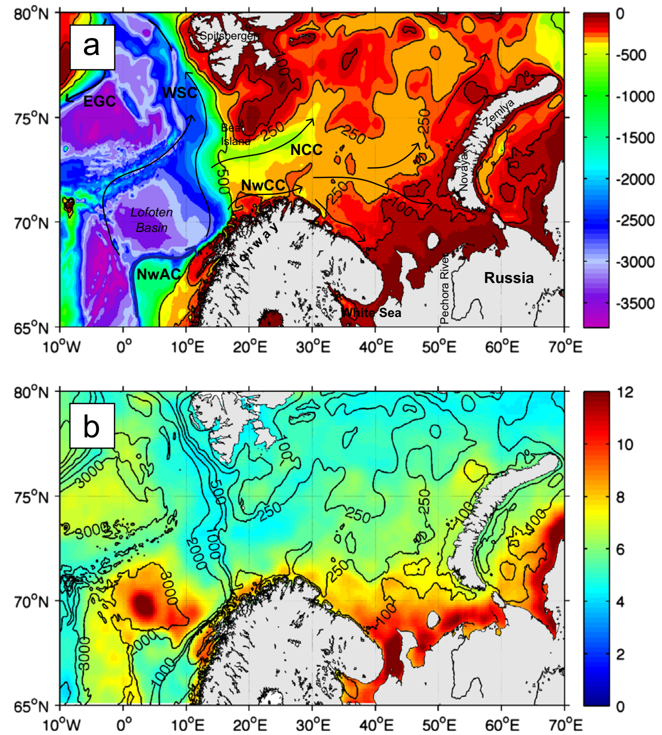

Fig. 1. (a) Bottom topography of the study domain (color) and major currents (arrows). (b) Standard deviation (cm) of SLA_T, measured with satellite altimetry. Contours show the bottom topography. Abbreviations: NwAC—Norwegian Atlantic Current, NCC—North Cape Current, NwCC—Norwegian Coastal Current, WSC—West Spitsbergen Current, EGC—East Greenland Current. (For interpretation of the references to color in this figure legend, the reader is referred to the web version of this article.)

oceanographic conditions in the BS (Furevik, 2001). Because of the AW inflow, the BS is never completely covered with sea ice, but the sea ice cover is subject to significant seasonal and interannual variability.

This paper aims to explore the causes of sea level variability in the BS. Sea level is an integral quantity that reflects (i) changes in the thermohaline properties of water masses, driven by the variations in buoyancy fluxes and advection by ocean currents, and (ii) changes in the mass of the water column, caused by the variations in wind forcing as well as the redistribution of water between the ocean, atmosphere, and land. Thus, the total sea level variability can be decomposed into the steric (expansion or contraction of water column due to the density variations) and mass-related sea level variability. The steric sea level variability can be further decomposed into the thermosteric and halosteric components.

Although the BS has been extensively surveyed over decades, the nature of the local sea level variability has not been adequately addressed. There have been a number of studies dedicated to the sea level variability in the Nordic seas (Mork and Skagseth, 2005; Steele and Ermold, 2007; Li et al., 2011; Richter et al., 2012), but only a few partially considered the BS (Proshutinsky et al., 2004, 2007; Volkov and Pujol, 2012; Henry et al., 2012; Calafat et al., 2013). Historically, sea level has been measured by tide gauges, the majority of which is located in the southern part of the BS along the Norwegian and Russian coasts. The BS tide gauges have been combined with other tide gauges along the Russian Arctic coast by Proshutinsky et al. (2004, 2007) to study the variability of sea level in the entire Arctic Ocean. Henry et al. (2012) analyzed the linear trends in tide gauge data along the Norwegian and Russian coasts and found an important contribution of the mass related change. Calafat et al. (2013) also analyzed the tide gauge records and explained the observed near-shore sea level variability by wind forcing and poleward propagation of sea level anomalies.

The advent of satellite altimetry has greatly advanced sea level studies by providing nearly global sea level measurements (Fu and Cazenave, 2001). From 1991 to 2012 the European Space Agency's satellites ERS-1, ERS-2, and Envisat were measuring sea level between 82°S and 82°N, thus completely covering the BS. Because of the ongoing long-term decrease of sea ice cover in the Arctic Ocean (Comiso et al., 2008), the sea ice edge in the BS is also retreating northeastward (Lebedev et al., 2011), which has made most of the BS area available for altimetry measurements. Lebedev et al. (2011) performed calibration and validation of satellite altimetry measurements in the BS and demonstrated its usefulness for local environmental monitoring. Volkov and Pujol (2012) showed that the quality of the recent global satellite altimetry product, distributed by AVISO (www.aviso.oceanobs.com), is adequate to study the synoptic and large-scale variability of sea level in the Nordic and Barents seas. The authors also estimated the amplitudes and phases of the annual cycle in the area and noted that the annual maximum sea level in the BS occurs 1–3 months later than in the Nordic seas. The launch of GRACE twin satellites in 2002 brought new perspectives of studying the variability of ocean mass (Chambers, 2006a, 2006b).

In this study, we aim to fill remaining gaps in the understanding of the mechanisms of local sea level changes. In particular, we want to (i) investigate the relative contribution of steric and mass effects to the regional sea level variability, (ii) explain the phase lag between the annual cycle in the BS and the neighboring Norwegian and Greenland seas, and (iii) study the role of wind forcing, net surface heat flux, and heat advection as drivers of the BS sea level variability. Hereafter, we use the following nomenclature for sea level anomaly (SLA) components: the total sea level anomaly (SLA_T), the mass-related sea level anomaly (SLA_M), the steric sea level anomaly (SLA_S), the thermosteric sea level anomaly (SLA_{TS}), and the halosteric sea level anomaly (SLA_{HS}).

2. Observational and modeled data

2.1. Satellite altimetry measurements

We use the AVISO maps of SLA_T from October 1992 to April 2012, generated by merging multi-satellite altimetry data. The high-latitude (above 66°) data are based on either ERS-1/2 or Envisat measurements. The data are corrected for instrumental errors, geophysical effects, tidal influence, and atmospheric wind and pressure effects, and objectively interpolated to a 1/3° Mercator projection grid (Le Traon et al., 1998). A dynamic atmospheric correction is applied to reduce the aliasing of the high-frequency sea level variability, especially in coastal regions (Carrere and Lyard, 2003; Volkov et al., 2007). Although the separation between the satellite's ground tracks and the ERS-1/2 and Envisat 35-day repeat period limits the resolution of eddy variability, the convergence of the ground tracks at high latitudes provides sufficient spatial and temporal coverage to adequately resolve the synoptic-scale variability in the Nordic and Barents seas (Volkov and Pujol, 2012).

Displayed in Fig. 1b is the standard deviation of SLA_T in the BS and in the neighboring areas. The maximum variability of SLA_T reaching about 15 cm is observed in the Lofoten Basin of the Norwegian Sea. It has been shown that among other factors this variability is largely due to the cyclonic propagation of topographic Rossby waves (Volkov et al., 2013). In the BS, the maximum SLA_T variability of 8–12 cm is observed in the south, over the shallow areas along the continent. The SLA_T variability gradually decreases down to 4–5 cm towards the northern boundary of the BS.

2.2. Ocean mass from GRACE

For SLA_M, we use gravity anomalies observed with the Gravity Recovery and Climate Experiment (GRACE), based on spherical harmonics from the Center for Space Research of the University of Texas and distributed as a $1^\circ \times 1^\circ$ gridded product via the GRACE Tellus website at Jet Propulsion Laboratory (http://grace.jpl.nasa.gov/). The processing of the monthly GRACE gravity observations and the derivation of ocean mass changes is described in detail in Chambers and Bonin (2012). The GRACE project recently released a re-processed data set (Release-05, RL05), which features (among several other updates) a new version of the ocean de-aliasing model (OMCT; Thomas, 2002) to remove high-frequency bottom pressure changes during processing. Chambers and Bonin (2012) found that overall RL05 has lower noise levels than RL04 (Release-04).

Spatially, uncertainties of ocean mass are larger toward high latitudes, where 1-sigma errors on the monthly ocean mass changes can be up to 1.5 to 2 cm. Using the error estimation of Wahr et al. (2006), we found an uncertainty of 1.6 cm for the GRACE average over the Barents Sea, consistent with Chambers and Bonin (2012). While no in-situ observations of bottom pressure exist in the Barents Sea, it has been shown that GRACE can reliably observe Arctic Ocean mass changes. Chambers and Bonin (2012) found good agreement between GRACE and in-situ bottom pressure recorders near the North Pole. In addition, we compared GRACE SLA_M against bottom pressure recorders in the Fram Strait (just west of Spitsbergen) between 2003 and 2009, and found local correlations of 0.6, with similar values throughout most of the interior Arctic Ocean as well as the Nordic seas (not shown). Although ocean bottom pressure and mass changes have a much smaller signal-to-noise ratio than water storage variations over land, GRACE can observe these variations.

GRACE satellites do not see changes of sea level induced by local atmospheric pressure variations. However, because water is incompressible, GRACE data need to be corrected for the globally averaged atmospheric pressure, i.e. global inverted barometer (IB) correction. We compute the global IB correction using the monthly mean sea level pressure from ERA-Interim reanalysis (Dee et al., 2011) and subtract it from GRACE SLA_M. The global IB correction varies predominantly on the seasonal time scale with a standard deviation of about 0.5 cm and is expected to have a significant impact on the annual cycle of SLA_M in the BS.

2.3. Hydrographic measurements

To investigate the role of steric effects in the variability of sea level in the BS, we use the vertical profiles of temperature and salinity from the hydrographic database of the Arctic and Antarctic Research Institute (St. Petersburg, Russia, www.aari.ru). These profiles are mostly represented by discrete measurements at standard depth levels (0, 5, 10, 15, 25, 50 etc.). In total, we use measurements from 33,516 irregularly spaced oceanographic stations (including 23,912 profiles with salinity measurements) carried out from 1950 to 1995 (Fig. 2). The period of 1950–1995 was chosen as the most covered with ship-based, nearly all-year-round oceanographic surveys and, hence, the parameters of the annual cycle can be considered as having no or little seasonal bias.

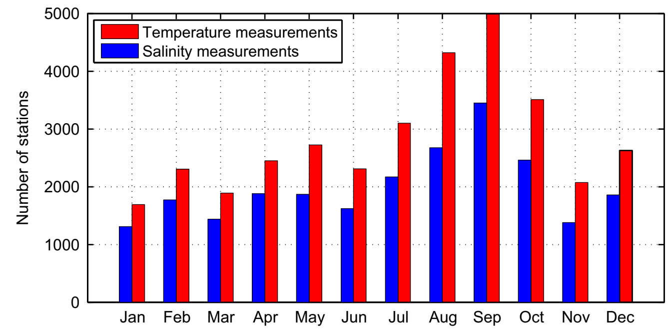

Fig. 2. The number of temperature and salinity profiles over the 25°E–45°E and 73°N–77°N area in each month during the 1950–1995 time interval, used for the computation of monthly mean climatology.

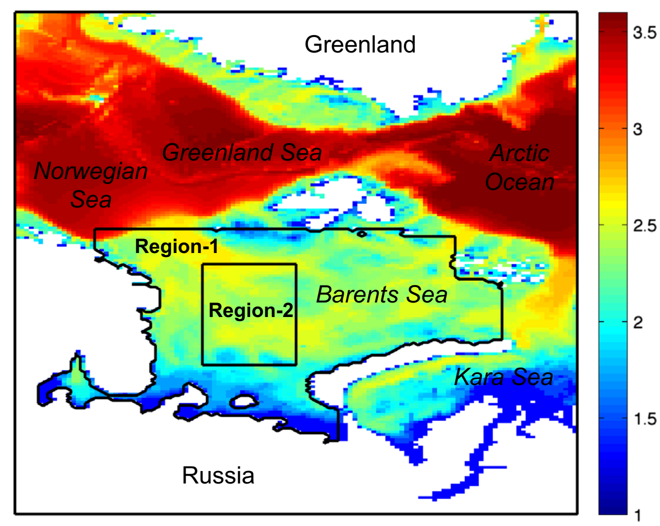

Fig. 3. The truncated ECCO2 model domain that we used in this study. Color shows the $\log_{10}$ of depth and two black contours bound the areas, over which averaging of quantities was performed: the entire Barents and White seas (Region-1) and the central part of the Barents Sea (Region-2). (For interpretation of the references to color in this figure legend, the reader is referred to the web version of this article.)

2.4. ECCO2 ocean data synthesis

To investigate the sea level budget of the BS we use an ECCO2 (Estimating the Circulation and Climate of the Ocean, Phase II) ocean data synthesis product. An ECCO2 data synthesis is obtained by least-squares fit of a global full-depth-ocean and sea-ice configuration of the Massachusetts Institute of Technology OGCM (Marshall et al., 1997) to the available satellite and in-situ data. This least-squares fit is carried out for a small number of control parameters using a Green's function approach (Menemenlis et al., 2005a). The control parameters include initial temperature and salinity conditions, atmospheric surface boundary conditions, background vertical diffusivity, critical Richardson numbers for the Large et al. (1994) KPP scheme, air–ocean, ice–ocean, air–ice drag coefficients, ice/ocean/snow albedo coefficients, bottom drag, and vertical viscosity. Data constraints include sea level anomalies, time-mean sea level, sea surface temperatures, vertical temperature and salinity profiles, and sea ice concentrations, motion, and thickness. The solution requires the computation of a number of sensitivity experiments that are free, unconstrained calculations by a forward model. The experiments are designed to adjust the model parameters, forcing, and initial conditions. Then the model is run forward again using the adjusted parameters, free of any constraints, as in an ordinary model simulation. The global ECCO2 configuration is eddy permitting. The model's mean horizontal grid spacing is 18 km and it has 50 vertical layers with thicknesses ranging from 10 m at the surface to 456 m near the bottom. Bathymetry is based on a global one arc-minute grid from the General Bathymetric Charts of the Oceans (GEBCO).

We use both the monthly and 3-day averages of the model-simulated sea level, bottom pressure, velocities, temperature, salinity, wind stress, and net surface heat flux. The monthly averages are used for comparison with satellite altimetry and GRACE observations, while the 3-day averages are used to estimate the components of the local barotropic vorticity budget. The period of the model run used in this study is 16 years (from January 1992 to December 2007). This yields 192 monthly and 1947 3-day records at each grid point. Displayed in Fig. 3 is the truncated model domain that we used in this study. The contours bound the regions used for spatial averaging: the entire Barents and White seas (Region-1) and the central part of the BS (Region-2).

3. Methods

In this section, we briefly review the principles of sea level dynamics and describe how the observational and modeled data were processed. The main factors that determine the variability of sea level, not related to tides and to the static effect of atmospheric loading (inverted barometer), are deduced from the continuity equation:

$$\frac{1}{\rho}\frac{\partial\rho}{\partial t}+\nabla\times\mathbf{u}+\frac{\partial w}{\partial z}=P-E+R \tag{1}$$

where ρ is the sea water density, $\mathbf{u}$ is the vector of horizontal velocity, w is the vertical velocity, P—precipitation, E—evaporation, R—river runoff. Because the fresh water balance terms cause a nearly instantaneous and uniform sea level change over the ocean basin, these terms can be neglected for the temporal and spatial scales of our interest. Integrating Eq. (1) from the sea surface to the bottom and using the boundary conditions $w=\partial\mathrm{SLA_T}/\partial t$ at the surface ($z=0$) and $w=0$ at the bottom ($z=H$), we obtain

$$\frac{\partial SLA_T}{\partial t}=-\nabla\times(\overline{\mathbf{u}}H)-\int_{-H}^{0}\frac{1}{\rho}\frac{\mathrm{d}\rho}{\mathrm{d}t}\mathrm{d}z \tag{2}$$

where $\overline{\mathbf{u}}$ is the vertically averaged velocity and $\overline{\mathbf{u}}H$ is the vertically integrated transport. Eq. (2) states that sea level changes due to (i) the divergence of water mass (mass effect) and (ii) the contraction or expansion of water column because of the changes in its density (steric effect). Satellite altimetry measurements, corrected for the inverted barometer effect, provide estimates of SLA_T, which, according to Eq. (2), are the sum of the mass-induced (SLA_M) and the steric (SLA_S) sea level anomalies (SLA_T=SLA_M+SLA_S). Spatial averaging over the 25°W–45°W and 73°N–77°N area for the observational data and over Region-1 and Region-2 (Fig. 3) for the ECCO2 fields is performed for the comparison of time series. The choice of the averaging area for the observational data is dictated by the desire to filter out the synoptic variability not resolved by GRACE and to stay away from the coast where the contamination of GRACE ocean data by land signals is the largest.

In order to directly compare the altimetry-measured SLA_T and the GRACE-derived SLA_M we subtract the monthly mean climatology from both time series, computed as the multiyear (from 2003 to 2011) average value for each month. By doing so, we remove a large part of the steric variability that dominates the seasonal variability of SLA_T. Thus, we expect that the non-seasonal variability of SLA_T will be dominated by mass signals (except the interannual variability) and can be directly compared to the non-seasonal variability of SLA_M. It is worth mentioning that for the comparison between the concurrent altimetry-measured SLA_T and the GRACE-derived SLA_M, prior to the computation of the monthly mean climatology, we subtract the linear trend from both data sets. Therefore, our analysis does not account for (and is not contaminated by) the long-term contributions to the sea level variability from vertical land movements, thermal expansion of the oceans, or melting glaciers.

The estimates of SLA_S are obtained from hydrography data and the ECCO2 output as the sum of the thermosteric (SLA_{TS}) and halosteric (SLA_{HS}) components, computed from the vertical profiles of temperature (T) and salinity (S):

$$SLA_S=SLA_{TS}+SLA_{HS}=-\rho_0^{-1}\left(\int_{-H}^{0}\rho(T,\overline{S},z)\mathrm{d}z+\int_{-H}^{0}\rho(\overline{T},S,z)\mathrm{d}z\right) \tag{3}$$

where ρ_0=1027.5 kg m^{-3} is a reference density, and $\overline{T}$ and $\overline{S}$ are the time mean values of T and S. The separation into the thermosteric and halosteric heights is approximate due to the nonlinear nature of the equation of state. The integration of both the in situ and modeled data is performed over the entire depth range.

The variability of SLA_{TS}, averaged over an area A, is determined by the net surface heat flux and lateral advection of heat:

$$\frac{\partial SLA_{TS}}{\partial t}=\frac{\alpha\overline{Q_{NET}}}{\rho_0 C_P}+\frac{\alpha}{A}\int_{-H}^{0}\oint_l(\mathbf{u}T)\mathrm{d}l\mathrm{d}z \tag{4}$$

where $\overline{Q_{NET}}$ is the area averaged net surface heat flux (positive into the ocean), α is the thermal expansion coefficient, C_p is the specific heat capacity of seawater, and l is the contour bounding the area A.

One of the largest and most physically deterministic signals in the sea level variability is the annual cycle (SLA_{ANN}), which we approximate by a least-squares fit of a harmonic function with an annual frequency (ω) to the monthly mean climatology of SLA components:

$$SLA_{ANN}(t)=a\cos(\omega t+\varphi) \tag{5}$$

where a is the annual amplitude, ω is frequency, φ is phase, and t—time. The phase of the annual cycle is represented as the month of the yearly maximum of SLA_{ANN}.

The parameters (amplitude and phase) of the hydrography-based annual cycle of SLA_S, SLA_{TS}, and SLA_{HS} are estimated over the area 25°E–45°E and 73°N–77°N using the following methodology. First, the monthly temperatures and salinities are interpolated by the inverse-distance weighted method onto a regular 100 × 100 km grid for each year from 1950 to 1995. At prognostic grid nodes and for each month of the year the search radius is varied from 60 to 200 km depending on station density. Then, the obtained temperature and salinity values are further averaged over the entire region (24 grid nodes) for each month at every standard depth. The standard errors of the mean temperatures and salinities are calculated to quantify the uncertainties in the seasonal steric changes. Because the considered period of hydrographic measurements (1950–1995) does not overlap with the concurrent satellite altimetry and GRACE records (2003–2011), we assume that all parameters of the annual thermohaline changes are rather constant and not strongly conditioned by recent climatic changes. This assumption will be justified in the next section.

The interannual SLA time series are computed as running means with a time window of 1 year after the monthly mean climatology has been removed. To estimate the relative contribution of each component of the variability, we also compute their standard deviations and explained variance. The percentage of variance (σ) of a variable x, explained by another variable y, is computed as

$$\sigma=100\%\times\left(1-\frac{\mathrm{var}(x-y)}{\mathrm{var}(x)}\right) \tag{6}$$

4. Results

4.1. Components of sea level variability from observations

4.1.1. Annual cycle

The amplitude and phase of the annual cycle of the altimetry-measured SLA_T are estimated for the 1993–2011 monthly mean climatology (Fig. 4). The amplitude of the annual SLA_T (Fig. 4a) reaches 8–10 cm over shallow areas in the southern part of the BS. In the central and northern parts of the BS, the annual amplitude varies from 3 to 5 cm. The annual maximum is observed in

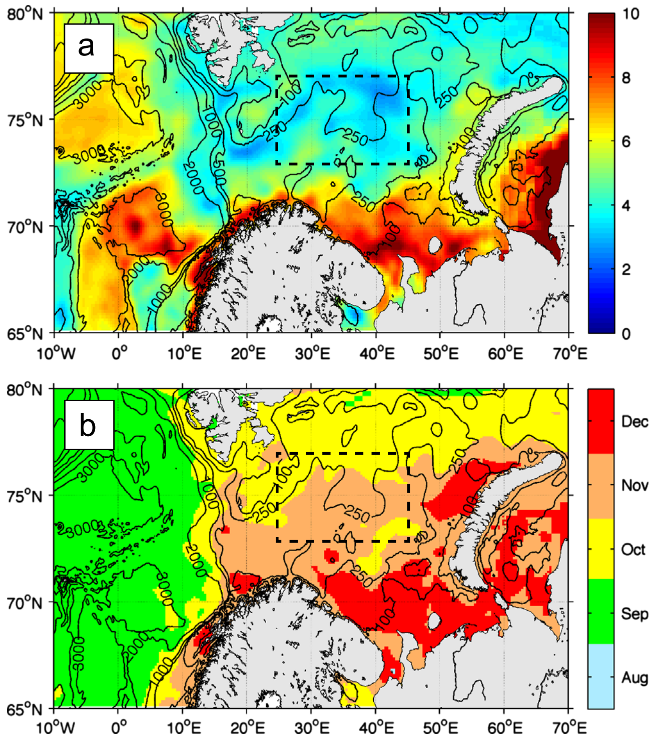

Fig. 4. (a) Amplitude (cm) and (b) phase (month of the annual maximum) of the annual cycle of altimetric SLA_T computed from the 1993–2011 monthly mean climatology. The dashed rectangle bounds the area used for averaging the time series.

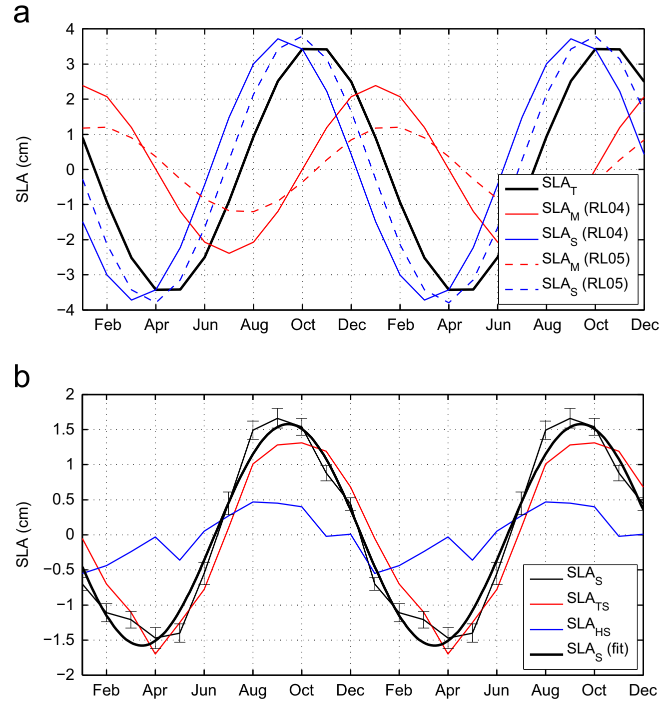

Fig. 5. (a) Annual cycles of SLA_T from satellite altimetry (black), SLA_M from GRACE RL04 (solid red) and RL05 (dashed red), and SLA_S, computed as the difference between SLA_T and GRACE-RL04 SLA_M (solid blue) and between SLA_T and GRACE-RL05 SLA_M (dashed blue). The time series of SLA_T and SLA_M are averaged over the 25°W–45°W and 73°N–77°N area (dashed rectangles in Fig. 4a and b). (b) Monthly mean climatology of steric (thin black), thermosteric (red), halosteric (blue) sea level anomalies, and the annual cycle of SLA_S (bold black), computed from hydrography data for the time period of 1950–1995 over the 25°W–45°W and 73°N–77°N area. The error bars show the standard errors on the determination of the monthly mean values at 95% confidence level. (For interpretation of the references to color in this figure legend, the reader is referred to the web version of this article.)

December in the southeastern and eastern (near the Novaya Zemlya archipelago) parts of the BS, and in October–November in the northern, western and central parts of the BS (Fig. 4b).

There is a sharp contrast between the occurrence of the annual maximum in the relatively shallow BS and in the neighboring Norwegian and Greenland seas. In the latter, the annual maximum is observed mostly in September, while in the BS it occurs from 1 to 3 months later. We hypothesize that the observed phase lag can be due to (i) the SLA_M variability due to the influence of wind, (ii) the SLA_S variability due to the variable advection of warm and saline AW from the Norwegian Sea and/or the regional impact of the net surface heat flux, and (iii) the impact of non-linear processes like large-scale propagating waves (e.g. Calafat et al., 2013). The variability of wind stress can affect the redistribution of water and, hence, bottom pressure, the inflow of the AW into the BS, and lead to the wind-induced changes in the baroclinic structure.

Displayed in Fig. 5a are the annual cycles of SLA_T and SLA_M, estimated for the 2003–2011 time interval common for satellite altimetry and GRACE measurements, and averaged over 25°E–45°E and 73°N–77°N in the center of the Barents Sea. The annual amplitude of SLA_T is about 3.5 cm. It appears that in RL05 data the annual cycle of SLA_M is about two times smaller than in RL04 data: the annual amplitude of SLA_M is about 2.4 cm in RL04 and only about 1.2 cm in RL05. The annual maximum of SLA_M in RL04 data occurs in January (in February in RL05 data), while the annual maximum of SLA_T is observed in November. If the space-borne observations did not contain errors, the time series of SLA_S could be computed by subtracting SLA_M from SLA_T. If we do so for SLA_M, the annual amplitude of SLA_S is about 3.8 cm for both RL04 and RL05 data products and the annual maximum is observed in September–October (Fig. 5a, blue solid and dashed curves). These observations thus indicate a 3-month lag between the annual maxima of SLA_S and SLA_M. The phase of SLA_T is determined by the interference of the steric and mass components. It should be noted that the amplitude of SLA_S, computed as the difference of SLA_T and SLA_M, is highly sensitive to their phases.

Table 1
The amplitudes (A, cm) and phases (φ, months of the annual maximum) of the annual cycle of SLA_S, SLA_{TS}, and SLA_{HS} for three time intervals: 1950–1995, 1950–1965, and 1980–1995.

Time interval	SLA_S		SLA_{TS}		SLA_{HS}	
	A	φ	A	φ	A	φ
1950–1995	1.6	Sep	1.5	Oct	0.4	Aug
1950–1965	1.7	Sep	1.5	Oct	0.8	Aug
1980–1995	1.6	Sep	1.2	Oct	0.6	Aug

To validate the estimates of the annual cycle of SLA_S, obtained from altimetry and GRACE measurements, we present the monthly mean climatology of SLA_S, calculated for the 1950–1995 time interval and averaged over 25°W–45°W and 73°N–77°N (Fig. 5b, black curve; Table 1). The annual amplitude and phase of SLA_S are obtained by fitting a harmonic function with an annual frequency (Fig. 5b, bold black curve). The amplitude of the annual SLA_S, estimated from hydrography, is 1.6 cm, which is about two times smaller than the amplitude of the annual SLA_S estimated from altimetry and GRACE (Fig. 5a). The annual maximum of the hydrography-derived SLA_S is observed in September, which is close to that estimated from altimetry and GRACE RL04 data. If we subtract the hydrographic SLA_S from SLA_T, we obtain SLA_M with annual amplitude of 2.3 cm and maximum in December. The closer agreement between these estimates and GRACE RL04 in terms of the amplitudes and phases (in contrast to GRACE RL05) indicates that GRACE RL05 potentially attenuates the annual cycle of SLA_M in the BS. In an attempt to resolve these discrepancies, we investigated differences over the study region of the monthly mean de-aliasing OMCT models used in the GRACE processing. While the RL04 and RL05 OMCT models differ over the study region (RMS of 1.4 cm between 2003 and 2011, detrended), the RMS differences between the RL04 and RL05 SLA_M is larger (1.8 cm). This indicates that other GRACE processing steps or parameters contribute to the differences, or that residual sub-monthly variability (not properly resolved in OMCT) is aliased into the monthly gravity fields. The discrepancies between RL04 and RL05 are most prominent for the annual cycle, but much less pronounced for the non-seasonal variations (see next section).

Using hydrography data we also estimate the thermosteric and halosteric contributions to SLA_S (Fig. 5b; Table 1). The amplitude of SLA_{TS} is about three times greater than the amplitude of SLA_{HS}. The annual maximum of SLA_{TS} is observed in October when the heat content of seawater reaches its highest value. The annual maximum of SLA_{HS} is observed in August. This is possibly related to the annual minimum of salinity transport from the Norwegian Sea due to the influence of the continental runoff that during the spring–summer period reduces the salinity of the NwAC. The spring–summer melt of sea ice in the BS may also contribute to the SLA_{HS} maximum in August, especially during the 1950–1995 time interval when the seasonal ice cover was larger than today.

To justify the previously made assumption that the parameters of the annual thermohaline changes do not change much over time, we present estimates of the amplitudes and phases of the annual cycle of SLA_S, SLA_{TS}, and SLA_{HS} separately for two 16-year time intervals: 1950–1965 and 1980–1995 (Table 1). The parameters of the annual cycle appear to be rather steady, especially for SLA_S. It should be noted, however, that errors on the determination of the annual cycle for each 16-year time interval are a priori larger than for the entire time interval. Also, the errors on the determination of the annual cycle of SLA_{HS} are larger than for the annual cycle of SLA_{TS}, because in each month of the year there are less salinity measurements than temperature measurements (Fig. 2). This is probably why the amplitude of the annual cycle of SLA_{HS} for the 1950–1995 interval significantly differs from the amplitudes for the 1950–1965 and 1980–1995 time intervals.

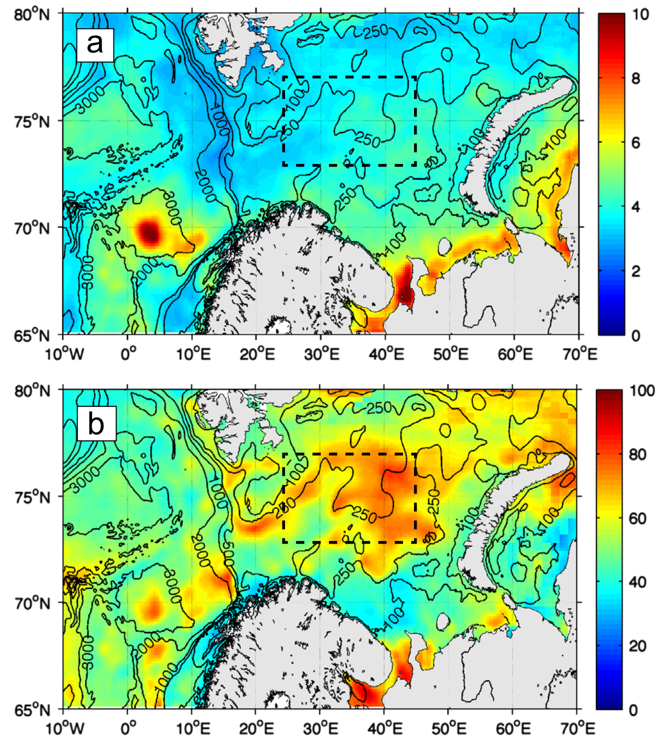

Fig. 6. (a) Standard deviation (cm) of the non-seasonal altimetric SLA and (b) its explained variance (%).

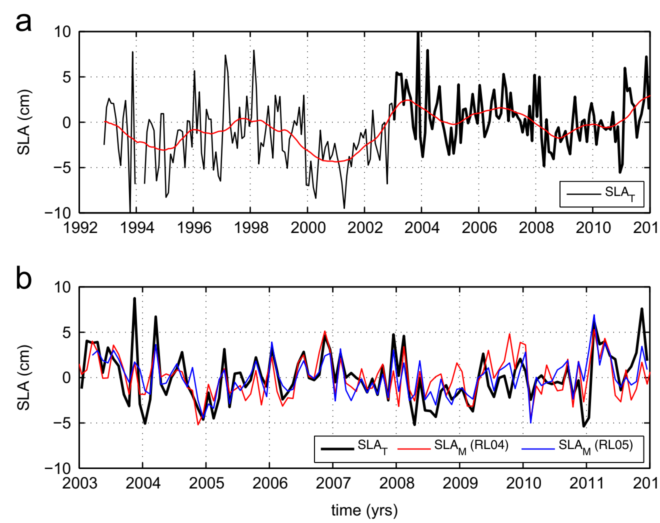

Fig. 7. (a) The non-seasonal SLA_T from satellite altimetry for the 1992–2011 time period (black) and it yearly running mean (red); (b) the de-trended time series of the non-seasonal SLA_T (black) versus SLA_M from GRACE RL04 (red) and RL05 (blue) products for the 2003–2011 time period. The time series are averaged over 25°W–45°W and 73°N–77°N. (For interpretation of the references to color in this figure legend, the reader is referred to the web version of this article.)

4.1.2. Non-seasonal variability

The non-seasonal SLA in both the satellite altimetry and GRACE data is obtained by subtracting the 2003–2011 monthly mean climatology. The standard deviation of the non-seasonal SLA_T in the BS (Fig. 6a) varies from about 3 cm in the western and northern parts to about 4–5 cm in the central and southeastern part of the sea. Along the Russian coast in the southeastern part of the BS, the standard deviation reaches 7–10 cm. The non-seasonal SLA_T variability explains 70–80% of the variance in the center of the BS (Fig. 6b). It is interesting to note that the relative contribution of the non-seasonal variability is largest approximately along the 250 m isobath in the central part of the BS. This is the area where Lien et al., (2013) reported on changes in barotropic flow induced by the cross-slope Ekman transport off the northern BS shelf. In the southern part of the BS the non-seasonal variability explains from 30% to 50% of the variance, while the rest is contributed by the annual cycle.

Displayed in Fig. 7 are the time series of the non-seasonal SLA_T and SLA_M, averaged over 25°W–45°W and 73°N–77°N. The non-seasonal SLA_T manifests substantial interannual variability over the 1993–2011 time interval (Fig. 7a). The standard deviation of the non-seasonal SLA_T is 3.5 cm, while the standard deviation of its running mean with a time window of 1 year is 2 cm. The standard deviation during the 2003–2011 time interval (2.8 cm), common for altimetry and GRACE measurements, is smaller compared to the preceding time interval (3.5 cm). For the comparison between the non-seasonal SLA_T and SLA_M over the 2003–2011 time interval the linear trend was removed from both time series (Fig. 7b). As was done for the annual cycle, we consider the non-seasonal SLA_M for both the GRACE RL04 and RL05 datasets. The correlation between the time series is 0.75. The standard deviation of each is approximately 2 cm and the standard deviation of the difference between them is 1.5 cm. This means that the uncertainty of GRACE data in the region is rather large and without adequate regional validation it is impossible to tell which dataset is more reliable. Nevertheless, both the non-seasonal SLA_M time series from GRACE RL04 and RL05 are correlated with the non-seasonal SLA_T. The correlation coefficients

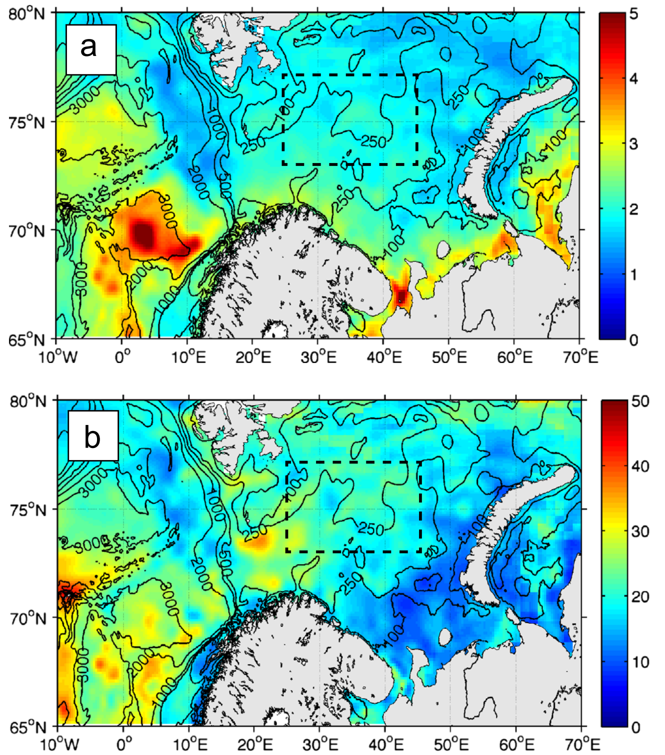

Fig. 8. (a) Standard deviation (cm) of the interannual SLA_T from satellite altimetry and (b) its explained variance (%).

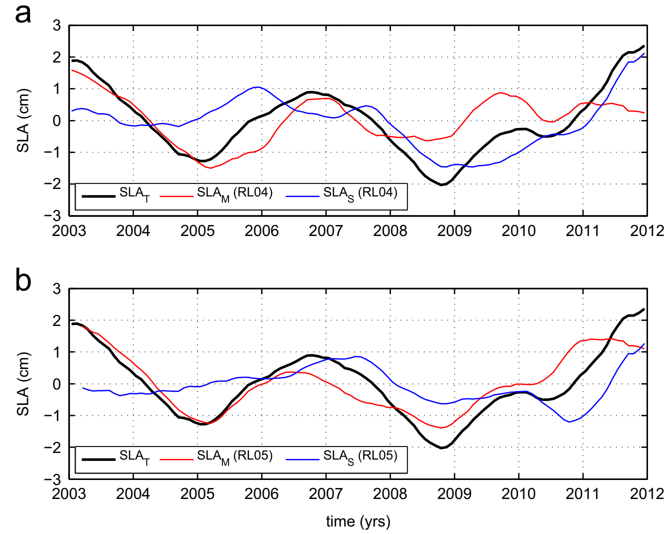

Fig. 9. The yearly running means of the de-trended non-seasonal SLA_T (black curves), SLA_M (red curves), and $SLA_S = SLA_T - SLA_M$ (blue curves). The SLA_M time series are shown for GRACE RL04 (a) and RL05 (b) data. The time series are averaged over 25°W–45°W and 73°N–77°N. (For interpretation of the references to color in this figure legend, the reader is referred to the web version of this article.)

are 0.62 and 0.71, respectively, significant at 95% confidence. Computed using Eq. (6), the non-seasonal variability of SLA_M in RL04 and RL05 explains 35% and 50% of the non-seasonal SLA_T variability, respectively. As a complement to previous modeling (e.g. Bingham and Hughes, 2012), this is the first observational evidence of the importance of the mass-related intra-seasonal variability of sea level in the BS.

4.1.3. Interannual variability

The interannual SLA_T and SLA_M are calculated as running means of the non-seasonal SLA_T and SLA_M with a 1-year window. The interannual variability of SLA_T in the BS is relatively small compared to the neighboring Norwegian and Greenland seas (Fig. 8a). Its standard deviation generally ranges between 1 and 2 cm. Only in the southern part of the BS along the coast, the standard deviation of the interannual SLA_T reaches 4–5 cm. The interannual SLA_T variability (Fig. 8b) explains 30–35% of the non-seasonal SLA_T variance near the western boundary, at the location, where most of the AW inflow takes place. Then, the explained variance gradually decreases towards the east and the southeast of the BS.

The interannual SLA_T (Fig. 9, black curve) and SLA_M from GRACE RL04 (Fig. 9a, red curve) and RL05 (Fig. 9b, red curve) datasets, averaged over 25°W–45°W and 73°N–77°N, show that the variability of SLA_M plays an important role at the interannual time scale. As suggested by both the RL04 and RL05 datasets, during the 2003–2005 time interval the contribution of SLA_S, computed as the difference between SLA_T and SLA_M, was rather small compared to the contribution of SLA_M. After 2005 the contribution of SLA_S became comparable to the contribution of SLA_M.

4.2. Components of sea level variability from ECCO2

4.2.1. Total, mass, and steric sea level variability

The advantage of using a model over observations is the easiness to accurately estimate the components of sea level budget. Unlike the space-borne and in situ measurements, the model data are free of sampling errors, the aliasing of unresolved signals, the contamination by land signals, etc. The advent of ocean models constrained by observations, like ECCO2, opens new perspectives in studying ocean dynamics (Menemenlis et al., 2005b). In the ECCO2 model, SLA_M is derived from the bottom pressure output and SLA_S is simply given by the difference SLA_T–SLA_M.

In Fig. 10a–c, we show the standard deviations of the monthly SLA_T, SLA_M, and SLA_S, calculated from the ECCO2 output. Although the ECCO2 model somewhat underestimates the SLA_T variability, its spatial distribution is similar to that in satellite altimetry data (compare Fig. 10a and Fig. 1b). The maximum variability of SLA_T in the BS is observed along the Russian coast and it exceeds 7 cm. In the central part of the BS the variability of SLA_T is about 5 cm, which is the same as observed by satellite altimetry. The maximum variability of SLA_M is also observed along the coast and in the center of the BS it reaches nearly 4 cm (Fig. 10b). The variability of SLA_S in the BS is relatively small and varies from about 1 to 3 cm (Fig. 10c), mainly on the seasonal time scale (not shown). Its maximum values of about 5 cm are observed along the NwAC near the western boundary of the BS. It appears that SLA_M explains most of the variance of SLA_T in the BS (Fig. 10d). In the central, eastern, and southern parts of the BS, SLA_M explains 70–90% of the variance. In the northern part it explains 50–80% of the variance. Near the western boundary, in the area where the AW enters the BS, SLA_M explains only 30–50% of the SLA_T variance suggesting the dominance of steric signals in this advective region.

Using Eq. (3) we estimate contributions of the thermosteric and halosteric effects to the SLA_S variability from the ECCO2-simulated monthly fields of temperature and salinity. The standard deviations of SLA_{TS} (Fig. 11a) generally depict the distribution of the AW in the Nordic seas and its further transport into the Arctic Ocean. In the BS, there are two distinct branches carrying AW: the North Cape Current and the Norwegian Coastal Current. Along these currents the standard deviation of the SLA_{TS} variability reaches 2–3 cm. Over most part of the BS, the standard deviations of SLA_{HS} do not exceed 1.5 cm (Fig. 11b). The minimum SLA_{HS} variability takes place along the North Cape Current. Along the Norwegian Coastal Current that is more influenced by the continental runoff, the standard deviations of SLA_{HS} exceed 2 cm. In the southeastern part of the BS and in the other regions subject to the seasonal sea ice formation and continental runoff the

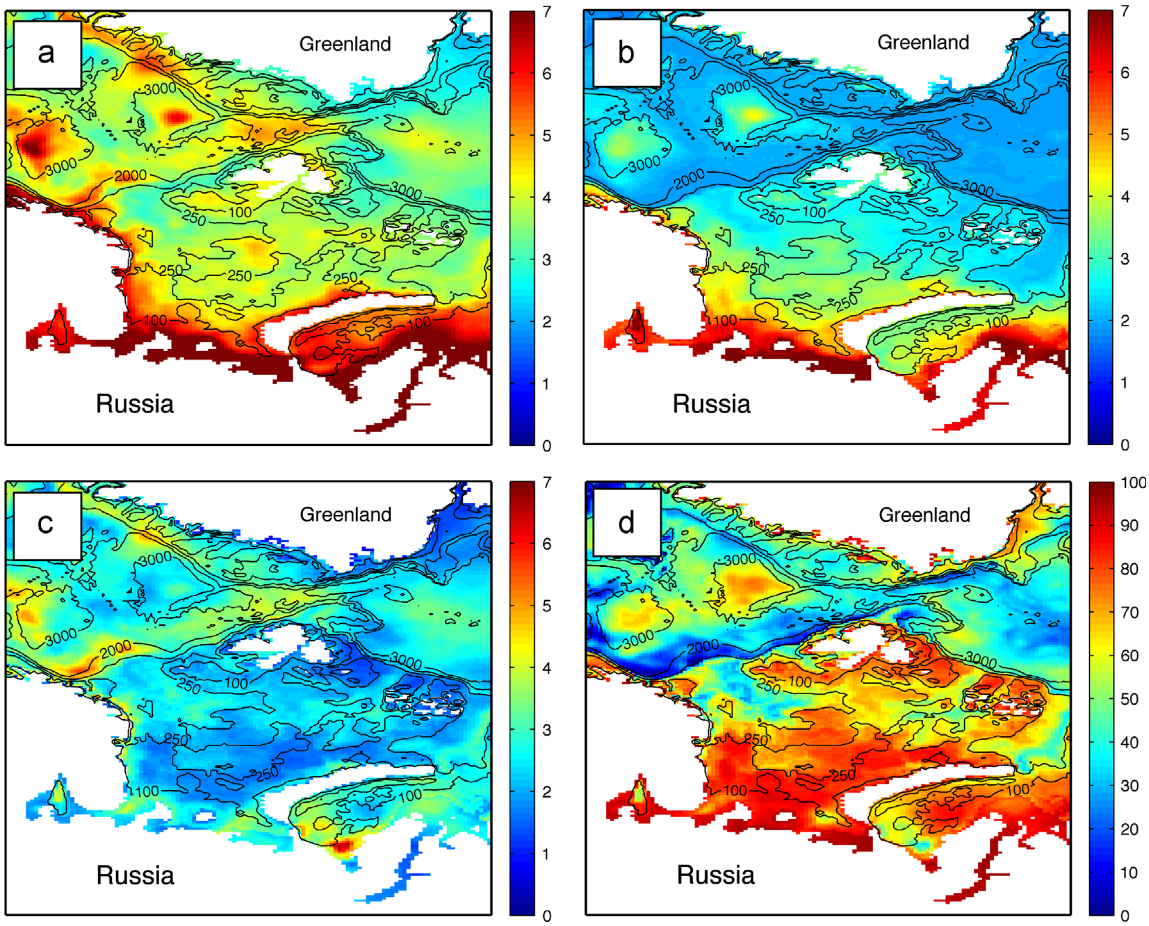

Fig. 10. Standard deviations (cm) of SLA_T (a), SLA_M (b), and SLA_S (c). (d) Variance explained by SLA_M (%) in the ECCO2 model. Bottom topography is shown for 100, 250, 1000, 2000, and 3000 m.

standard deviations of SLA_{HS} exceed 3 cm. The SLA_{TS} variability explains most of the SLA_S variance in the western, central, and southern parts of the BS (Fig. 11c), while the SLA_{HS} variability dominates in the southeastern, northern, and eastern parts of the BS (Fig. 11d), where the seasonal sea ice formation takes place. This suggests that the salinity advection from the Norwegian Sea does not strongly impact the SLA_{HS} in the BS.

4.2.2. *Annual cycle*

The amplitudes and phases of the annual cycle of SLA_T, SLA_M, and SLA_S are presented in Fig. 12. The maximum annual amplitude of SLA_T reaching 8–10 cm is observed along the Russian coast, while in the central part of the BS the amplitude is about 3–4 cm (Fig. 12a). This compares well with the annual amplitude estimated from satellite altimetry (Fig. 4a). The agreement between the annual phases estimated from the ECCO2 model (Fig. 12d) and from satellite altimetry measurements (Fig. 4b) is also satisfactory. Similar to satellite altimetry, the ECCO2 model also exhibits a 1–3 month phase lag between the BS and the adjacent areas to the west. In the ECCO2 model, the annual maximum of SLA_T takes place in October–December in the BS and in September–October in the Nordic seas. The annual amplitude of SLA_M (Fig. 12b) is several times larger than the annual amplitude of SLA_S (Fig. 12c) along the coast.

In the central part of the BS (Region-2 in Fig. 3), the annual amplitude of SLA_M is 1.8 cm, while the annual amplitude of SLA_S is 2.2 cm (Fig. 13a). These estimates reasonably match the ones we obtained from GRACE RL04 (Fig. 5a) and from hydrography data (Fig. 5b). The annual cycle of SLA_S in the area is mostly due to the thermosteric variability (Fig. 13b). The amplitude of SLA_{TS} is about 1.7 cm, while the amplitude of SLA_{HS} is 0.3 cm. These numbers are also close to those obtained from hydrography data (see Fig. 5b). Therefore, these comparisons suggest that the ECCO2 model adequately reproduces the annual cycle and can be used to investigate the reason for the observed phase lag between the BS and the Nordic seas.

As we mentioned earlier, the lag can be caused by the advection of warm and saline AW from the Norwegian Sea, by wind, by variations of the net surface heat flux, or by non-linear processes like the propagation of large-scale waves. So, the first question we need to answer is whether the lag is caused by mass-related or steric signals. As revealed by the annual phases of SLA_M, and SLA_S (Fig. 12e and f), only the mass-related variability manifests a distinct phase difference between the BS and the Nordic seas. The annual phase of the steric variability is distributed rather uniformly suggesting that neither the anomalies in the AW inflow nor the variations of the net surface heat flux are responsible for the delay of the annual maximum of sea level in the BS compared to the neighboring Nordic seas.

4.2.3. *Forcing of mass-related variability*

In this section we investigate the mechanisms driving the mass-related variability of sea level in more detail by analyzing the barotropic vorticity balance in the central part of the BS. The barotropic vorticity equation for the depth-integrated flow is expressed as follows:

$$\frac{\partial \zeta}{\partial t} + \mathbf{u}\nabla\zeta + \beta v - \frac{\zeta + f}{H}\left(\frac{\partial SLA_M}{\partial t} + \mathbf{u}\nabla H\right) = \frac{1}{\rho}\nabla \times \left(\frac{\boldsymbol{\tau}}{H}\right) - D \qquad (7)$$

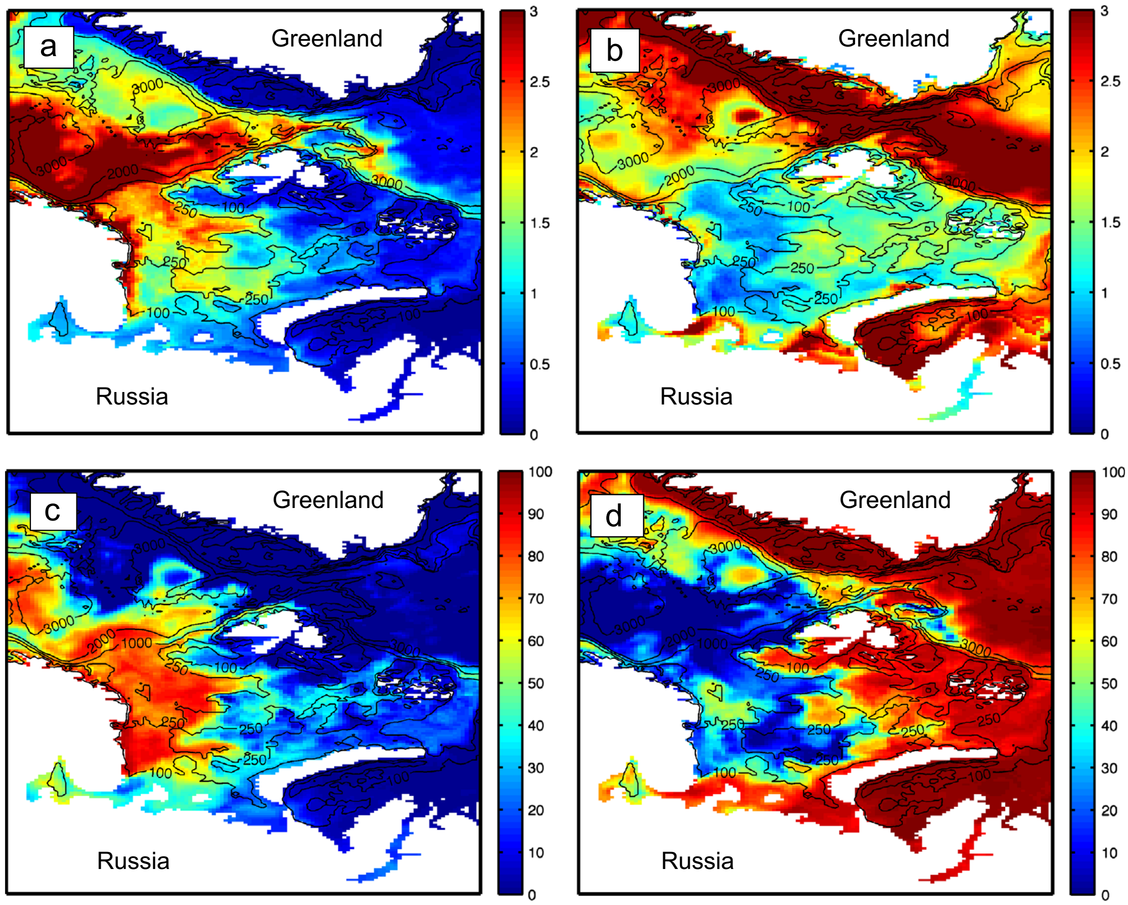

Fig. 11. The standard deviations of the thermosteric (a) and halosteric (b) sea level, and the portion of the SLA_S variance explained by the thermosteric (c) and halosteric (d) signals. Bottom topography is shown for 100, 250, 1000, 2000, and 3000 m.

where H is depth, $\mathbf{u}(u,v)$ is the depth-integrated velocity vector, f is the planetary vorticity, $\zeta = \partial v/\partial x - \partial u/\partial y$ is the relative vorticity, $\beta = \partial f/\partial y$, $\boldsymbol{\tau}(\tau_x,\ \tau_y)$ is the wind stress vector, ρ is density, and D—dissipation. The left side of Eq. (7) represents the sum of the time change of the relative vorticity, the advection of the relative vorticity tendency, the advection of planetary vorticity, (in brackets) the vortex stretching term and the topographic term (representing the flow over the varying topography). The right side of Eq. (7) contains forcing: the wind stress term and dissipation. Because we are interested only in the wind-induced changes of SLA_M ignoring the freshwater balance, the mass-related variability of sea level is computed as the divergence of the depth integrated flow:

$$\frac{\partial SLA_M}{\partial t} = -\nabla \times (\mathbf{u}H) \tag{8}$$

The terms on the left side of Eq. (7) and the wind stress term are calculated directly from the ECCO2 output. These terms are averaged over the Region-2 (Fig. 3) away from the coast in order to minimize friction. The use of the 3-day averaged data does not allow us to accurately estimate the nonlinear terms, namely the advection of the relative vorticity tendency and dissipation, because the contribution of the variability with periods shorter than 3 days is ignored. By assuming that this contribution is small, we estimate the dissipation term as the residual of all other terms in Eq. (7).

Displayed in Fig. 14 is a zoom-in on the 2000–2003 time interval showing the sum of the left side terms (black curve), the wind stress term (red curve), and the dissipation term of Eq. (7) (blue curve). The sum of the left side terms is almost fully balanced by the wind stress term. The balance is mostly due to the topographic and wind stress terms that are on average more than an order of magnitude larger than the remaining terms on the left side of the Eq. (7), so that

$$-\frac{\zeta+f}{H}(\mathbf{u}\nabla H) \approx \frac{1}{\rho}\nabla \times \left(\frac{\boldsymbol{\tau}}{H}\right) - D \tag{9}$$

The variability of the dissipation term is about two times smaller than the topographic and wind stress terms (Fig. 14), but greater than the remaining terms. The absolute value and the variability of dissipation are largest during the winter months when the magnitude and fluctuations of wind stress are the strongest.

From Eq. (7) the variability of SLA_M is

$$\frac{\partial SLA_M}{\partial t} = k\frac{\partial \zeta}{\partial t} + k(\mathbf{u}\nabla\zeta + \beta v) - \mathbf{u}\nabla H - \frac{k}{\rho}\nabla \times \left(\frac{\boldsymbol{\tau}}{H}\right) + kD \tag{10}$$

where $k = H/(\zeta+f)$. The first three terms on the right side of Eq. (10) are of the same order of magnitude as the residual (consisting of the last three terms) and can be compared with $\partial SLA_M/\partial t$ (Fig. 15). The correlation coefficient between $\partial SLA_M/\partial t$ and $k \times \partial\zeta/\partial t$ is rather small ($r = -0.23$), but significant at 95% confidence for 1947 (length of time series) degrees of freedom. This means that when a cyclonic/anticyclonic circulation anomaly develops, sea level tends to decrease/increase (Fig. 15a). There is almost no relationship between $\partial SLA_M/\partial t$ and the advection of the relative vorticity tendency and $\partial SLA_M/\partial t$ and the advection of planetary vorticity (Fig. 15b and c). The correlation coefficient between $\partial SLA_M/\partial t$ and $k\mathbf{u}\nabla\zeta$ is 0.01 and between $\partial SLA_M/\partial t$ and $k\beta v$ is -0.14. Therefore, the impact of non-linear processes on the mass-induced variability of sea level in the central part of the BS

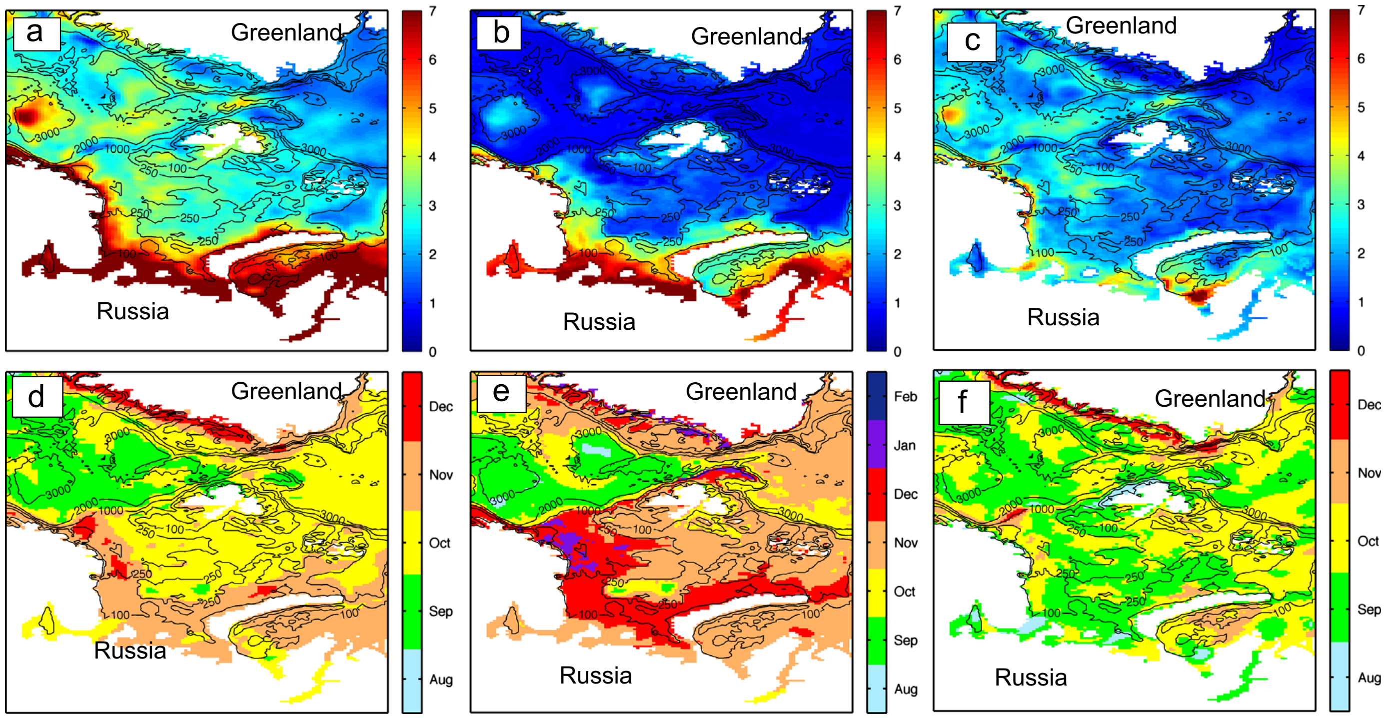

Fig. 12. The amplitudes (upper plots) and phases (lower plots) of the annual cycle of SLA_T ((a) and (d)), SLA_M ((b) and (e)), and SLA_S ((c) and (f)), obtained from the ECCO2 output. Bottom topography is shown for 100, 250, 1000, 2000, and 3000 m.

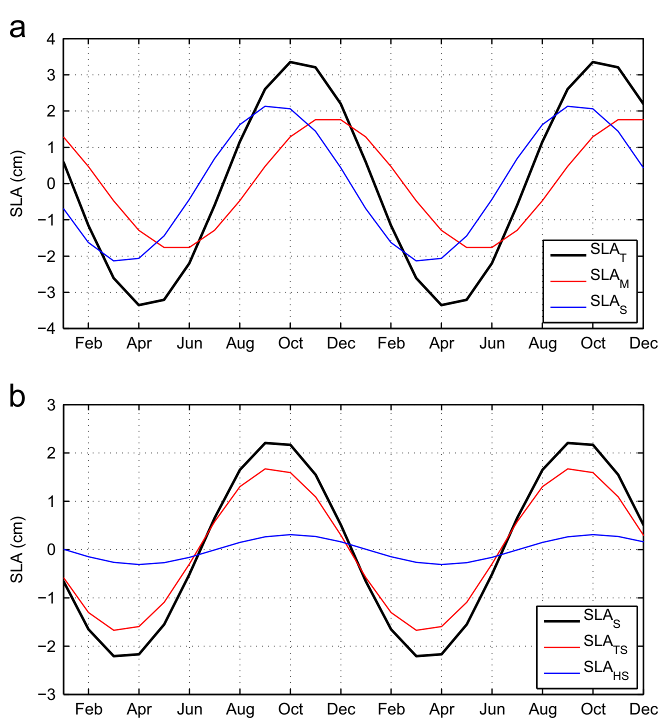

Fig. 13. (a) Annual cycles of SLA_T (black), SLA_M (red), and SLA_S (blue), and (b) annual cycles of SLA_S (black), SLA_{TS} (red), and SLA_{HS} (blue) from ECCO2 model. The time series are averaged over Region-2 (Fig. 3). (For interpretation of the references to color in this figure legend, the reader is referred to the web version of this article.)

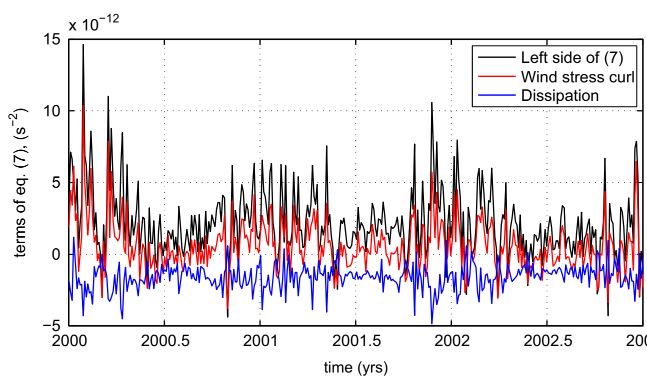

Fig. 14. Components of the barotropic vorticity budget averaged over Region-2 (Fig. 3): the sum of the left side terms of Eq. (7) (black), the wind stress term (red), and the dissipation term (blue). (For interpretation of the references to color in this figure legend, the reader is referred to the web version of this article.)

is probably negligible. What does determine the mass-related changes of sea level in the BS is the combined effect of wind stress, flow over the varying topography, and dissipation (Fig. 15d). The correlation coefficient between $\partial SLA_M/\partial t$ and $\{-\mathbf{u}\nabla H - k\rho^{-1}\nabla \times (\boldsymbol{\tau}/H) + kD\}$ is 0.8.

4.2.4. The role of heat fluxes

As was demonstrated earlier, the thermosteric effect dominates the SLA_S variability over a large part of the BS, affected by the advection from the Nordic seas (Fig. 11c). In this section, we use Eq. (4) to assess the role of the net surface heat flux and the lateral advection in the SLA_{TS} variability, simulated by the ECCO2 model.

Displayed in Fig. 16a are the time series of the time derivative of SLA_{TS} and the terms of the right side of Eq. (4) related to the net surface heat flux and heat advection by ocean currents averaged over the entire Barents and White seas (Region-1 in Fig. 3). It appears that most of the thermosteric sea level variability over the BS is determined by the net surface heat flux (red curve in Fig. 16a). The average net surface heat flux is negative meaning that on average the BS looses heat to the atmosphere. This average heat loss is compensated by heat advection from the neighboring Norwegian Sea (blue curve in Fig. 16a). The heat advection is always positive leading to the increase of the thermosteric sea

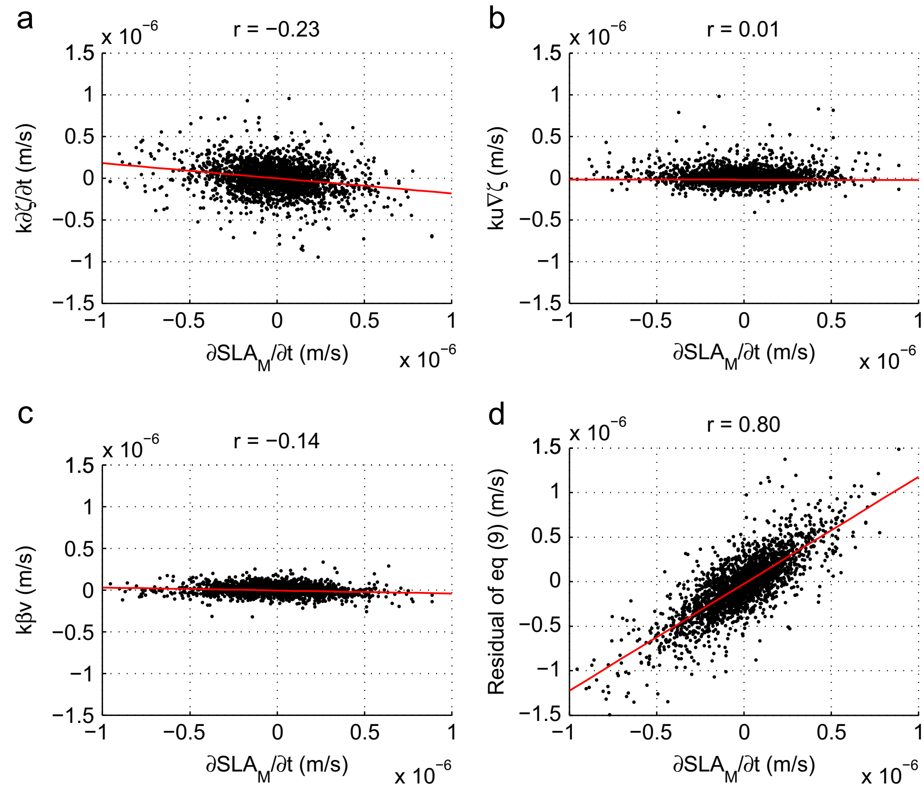

Fig. 15. Scatter plots of the terms in Eq. (10): (a) $\partial SLA_M/\partial t$ and $k\times\partial\zeta/\partial t$, (b) $\partial SLA_M/\partial t$ and $k\mathbf{u}\nabla\zeta$, (c) $\partial SLA_M/\partial t$ and $k\beta v$, and (d) $\partial SLA_M/\partial t$ and $-\mathbf{u}\nabla H - k\rho^{-1}\nabla\times(\boldsymbol{\tau}/H)+kD$. The terms of Eq. (10) are averaged over Region-2 (Fig. 3).

level in the BS. As expected, the annual cycle of the thermosteric sea level tendency is mostly driven by the net surface heat flux, which reaches a maximum value in June (Fig. 16b, red curve). Heat advection is also subject to small seasonal variations with annual amplitude of 0.5×10^{-7} cm/s and maximum in November (Fig. 16b, blue curve).

Although the variability of heat advection is several times smaller than the variability of the net surface heat flux, its contribution is particularly important at interannual time scales. The yearly averages of the terms of Eq. (4) (Fig. 16c) show that the interannual amplitude of heat advection exceeds the interannual amplitude of the net surface heat flux. The maximum increase of the model-simulated thermosteric sea level in 1999 was solely induced by the increase of heat advection. This result confirms the recent findings of Årthun et al. (2012), who also found a correlation between the inflow of heat and sea ice extent in the BS.

5. Discussion and conclusions

Climate change in the Arctic Ocean, where dramatic warming and decrease in sea ice cover is being observed, poses considerable concerns for society. Sea level is an integral indicator of climate variability. The BS is the only shelf sea of the Arctic Ocean that is mostly ice-free all year round, thus permitting regular satellite altimetry measurements. Coupling these measurements to GRACE and hydrography data, when measurement and processing errors are minimized, allows the determination of the sea level budget components. In this paper, we have presented one of the first attempts to analyze the local sea level budget using the combination of space borne and in-situ observations as well as a high-resolution ocean data synthesis product.

Using satellite altimetry and GRACE observations, we have presented the first observational evidence of the relative importance of the mass-related changes of sea level in the BS. We have shown that the non-seasonal mass-related changes of sea level are responsible for the large part (up to 50%) of the non-seasonal sea level variability in the BS. Significant contributions of the mass-related sea level variability, of the same magnitude or larger than the steric sea level variability, are also observed at interannual time scales. The difference of two GRACE data releases, however, highlights existing uncertainties, probably related to the processing algorithms of GRACE measurements and uncertainties in the high-frequency de-aliasing models used to estimate monthly GRACE gravity fields. We have shown that the recently released GRACE RL05 data attenuates the annual cycle signal compared to the previous RL04 product. By comparing the difference between the annual cycles of the altimetric SLA_T and GRACE-derived SLA_M to the hydrography-derived annual cycle of SLA_S and the ECCO2-derived annual cycles of SLA_M and SLA_S, we conclude that RL04 gives a more realistic result in the BS than the newer RL05. In terms of the non-seasonal variability, the standard deviation of the difference between the RL04 and RL05 time series, averaged over 25°W–45°W and 73°N–77°N, is 1.5 cm. These comparisons indicate that the uncertainties in GRACE data are still rather large and regional validation of GRACE products is warranted.

The phase of the annual cycle of SLA_T exhibits a distinct difference of 1–3 months between the BS and the neighboring Norwegian and Greenland seas. The annual cycle of SLA_T is the interference of the annual cycles of SLA_M and SLA_S. The analysis of GRACE observations shows that the annual maximum of SLA_M (from RL04) lags behind the annual maximum of SLA_T by three months. This suggests that the local importance of the mass-related sea level variability can be responsible for the observed phase difference between the BS and Nordic seas. To investigate this question in more detail, we have analyzed the mechanisms of the annual cycle in the ECCO2 model. It turns out that the phase

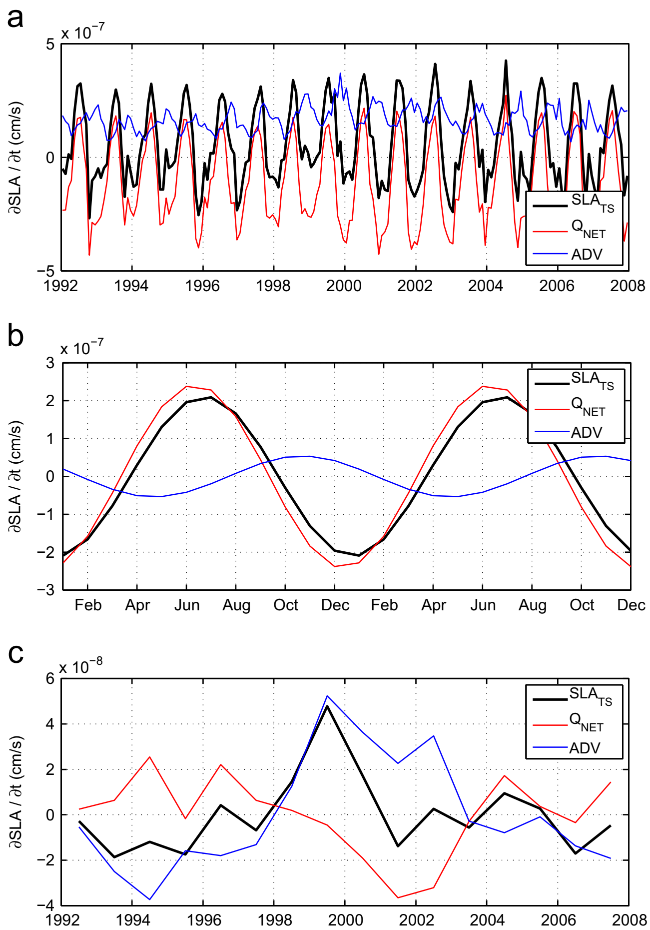

Fig. 16. The time change of the thermosteric sea level (black), thermosteric sea level due to the net surface heat flux (red), and thermosteric sea level due to the lateral advection (blue): (a) the monthly time series, (b) annual cycle, and (c) yearly averages. The time series shown are averaged over Region-1 (Fig. 3). (For interpretation of the references to color in this figure legend, the reader is referred to the web version of this article.)

of the annual cycle of SLA_S from ECCO2 is distributed rather uniformly over the BS and the Nordic seas. This rules out the possibility of the phase difference caused by the anomalous advection or the spatial variations in the net surface heat flux. The phase difference between the BS and the Nordic seas is seen only in the annual cycle of SLA_M.

The amplitude of the annual cycle of SLA_S, obtained as the difference between the altimetric SLA_T and GRACE-derived SLA_M, is about twice greater than the annual cycle of SLA_S, calculated from hydrographic data. This discrepancy is most likely caused by errors in GRACE data. We have demonstrated that the uncertainty of GRACE data, estimated as the difference between the two recent GRACE products, is rather large. The use of different time intervals for the satellite- and hydrography-based estimates of the annual cycle should not have a great impact. We have shown that the parameters of the annual cycle did not change much over the period of hydrographic surveys, considered in this study. In the ECCO2 model, the annual cycle of SLA_M in the central part of the BS is of about the same magnitude as the annual cycle of SLA_S. The amplitude and phase of the annual cycle of SLA_S in the model are rather close to the estimates, obtained from hydrography.

Because the mass-related variability of sea level is dominant in the BS, we have analyzed the barotropic vorticity balance in order to investigate the mechanisms of the barotropic variability in more detail. Neglecting the impact of fresh water fluxes to and from the BS, the variability of SLA_M is driven either by wind or by vorticity fluxes. We have shown that the advection of the relative vorticity tendency and the advection of planetary vorticity do not significantly influence the variability of SLA_M. What does drive the variability of SLA_M in the central part of the BS is the combined effect of wind forcing balanced by the flow over the varying bottom topography (topographic influence) and dissipation. The variability of wind stress curl over the BS forces water to flow in or out of the area thus changing the area-averaged sea level. With regard to the annual cycle, this means that the time-integrated cyclonic (anticyclonic) anomaly of wind stress observed in winter (summer) months (Fig. 14) leads to a decrease (increase) of sea level in the BS that reaches a minimum (maximum) in May–June (November–December) (Fig. 13a), i.e. several months after the actual maximum (minimum) in the wind stress curl anomaly, which is consistent with Ekman dynamics.

Using hydrography and the ECCO2 output we have estimated the contributions of the thermosteric and halosteric effects to the variability of sea level in the entire BS. As expected, the largest contribution of the thermosteric sea level in the BS is observed along the main paths of the AW advection: the North Cape Current and the Norwegian Coastal Current. The halosteric effects dominate in the southeastern, eastern, and northern parts of the BS, subject to the seasonal formation and melt of sea ice and to the river runoff. In terms of the annual cycle in the center of the BS, both the hydrography and ECCO2 data show the dominance of the thermosteric sea level with a maximum in the fall when the heat content of the water column reaches it highest value. The amplitude of the annual cycle of SLA_{HS} is about 3 times smaller than the amplitude of the annual cycle of SLA_{TS}. The annual maximum of the SLA_{HS} takes place at approximately the same time (August for hydrography and October for ECCO2), so that both signals complement each other. The halosteric sea level peaks along with the fresh water content due to the ice melt, continental runoff, and decreased salinity transport from the Norwegian Sea.

Using the ECCO2 output we have determined the relative contribution of the net surface heat flux and the lateral advection of heat to the variability of the thermosteric sea level. The variability of SLA_{TS} is dominated by the seasonal signal and, as expected, most of the variability is explained by heat exchange with the atmosphere. The contribution of heat advection to the annual cycle of SLA_{TS} is small. However, heat advection becomes important at the interannual time scale, when its contribution is equal or exceeds the contribution of the net surface heat flux. This means that the variability of the AW inflow into the BS on the interannual time scale can greatly influence the oceanographic conditions of the region, in particular, the regional extent of sea ice cover.

Acknowledgements

The altimeter products were produced by SSALTO/DUACS and distributed by AVISO with support from CNES (http://www.aviso.oceanobs.com/duacs/). GRACE ocean data were processed by Don P. Chambers, supported by the NASA MEASURES Program, and are available at http://grace.jpl.nasa.gov. The authors thank two anonymous reviewers for their comments and suggestions that helped to improve the manuscript. The ECCO2 model runs have been carried out at Jet Propulsion Laboratory, California Institute of Technology (http://ecco2.jpl.nasa.gov). DV and FL were supported by the NASA Physical Oceanography program. SK was supported by the Russian Federal Targeted program.

References

Årthun, M., Eldevik, T., Smedsrud, L.H., Skagseth, Ø., Ingvaldsen, R.B., 2012. Quantifying the influence of Atlantic heat on Barents Sea ice variability and

retreat. Journal of Climate 25 (13), 4736–4743, http://dx.doi.org/10.1175/JCLI-D-11-00466.1.
Bingham, R.J., Hughes, C.W., 2012. Local diagnostics to estimate density-induced sea level variations over topography and along coastlines. Journal of Geophysical Research 117, C01013, http://dx.doi.org/10.1029/2011JC007276.
Calafat, F.M., Chambers, D.P., Tsimplis, M.N., 2013. Interannual to decadal sea level variability in the coastal zones of the Norwegian and Siberian seas: the role of atmospheric forcing. Journal of Geophysical Research.
Carrere, L., Lyard, F., 2003. Modelling the barotropic response of the global ocean to atmospheric wind and pressure forcing—Comparisons with observations. Gephys. Res. Lett., 30, 1275–1278.
Chambers, D.P., Bonin, J.A., 2012. Evaluation of Release-05 GRACE time-variable gravity coefficients over the ocean. Ocean Science 8, 859–868, http://dx.doi.org/10.5194/os-8-859-2012.
Chambers, D.P., 2006a. Evaluation of new GRACE time-variable gravity data over the Ocean. Geophysical Research Letters 33 (17), LI7603.
Chambers, D.P., 2006b. Observing seasonal steric sea level variations with GRACE and satellite altimetry. Journal of Geophysical Research 111 (C3), C03010, http://dx.doi.org/10.1029/2005JC002914.
Comiso, J.C., Parkinson, C.L., Gersten, R., Stock, L., 2008. Accelerated decline in the Arctic sea ice cover. Geophysical Research Letters 35, L01703, http://dx.doi.org/10.1029/2007GL031972.
Dee, D.P., et al., 2011. The ERA-interim reanalysis: configuration and performance of the data assimilation system. Quarterly Journal of the Royal Meteorological Society, 137. John Wiley & Sons, Ltd., pp. 553–597.
Fu, L.-L., Cazenave, A., 2001. Satellite Altimetry and Earth Sciences: A Handbook of Techniques and Applications, Int. Geophys. Ser., vol. 69, Elsevier, New York.
Furevik, T., 2001. Annual and interannual variability of Atlantic Water temperatures in the Norwegian and Barents seas: 1980–1996. Deep Sea Research Part I: Oceanographic Research Papers 48, 383–404.
Henry, O., Prandi, P., Llovel, W., Cazenave, A., Jevrejeva, S., Stammer, D., Meyssignac, B., Koldunov, N., 2012. Tide gauge-based sea level variations since 1950 along the Norwegian and Russian coasts of the Arctic Ocean: contribution of the steric and mass components. Journal of Geophysical Research 117, C06023 http://dx.doi.org/10.1029/2011JC007706.
Large, W.G., McWilliams, J.C., Doney, S.C., 1994. Oceanic vertical mixing: a review and a model with a nonlocal boundary layer parameterization. Reviews of Geophysics 32, 363–403.
LeTraon, P.-Y., Nadal, F., Ducet, N., 1998. An improved mapping method of multi-satellite altimeter data. J. Atmos. Oceanic Technol., 15, 522–534.
Lebedev, S., Kostyanoy, A.G., Ginzburg, A.I., Medvedev, D.P., Sheremet, N.A., Shauro, S.N., 2011. Satellite altimetry applications in the Barents and White seas. In: Vignudelli, S., et al. (Eds.), Coastal Altimetry. Springer-Verlag, Berlin Heidelberg.
Li, L., Wang, H., Sun, R., 2011. Seasonal change of steric sea level in the GIN seas. Journal of Ocean University of China (English Edition) 10 (1), 16–22, http://dx.doi.org/10.1007/s11802-011-1762-0.
Lien, Vidar S., Vikebø, Frode B., Skagseth, Øystein, 2013. One mechanism contributing to covariability of the Atlantic inflow branches to the Arctic. Nature Communications 4, 1488, http://dx.doi.org/10.1038/ncomms2505.
Loeng, H., Sagen, H., Ådlandsvik, B., Ozhigin V., 1993. Current Measurements between Novaya Zemlya and Frans Josef Land September 1991–September 1992, Institute for Marine Research, Rep. no. 2, ISSN 0804-2128.
Marshall, J., Adcroft, A., Hill, C., Perelman, L., Heisey, C., 1997. A finite volume, incompressible Navier-Stokes model for studies of the ocean on parallel computers. Journal of Geophysical Research 102, 5753–5766, http://dx.doi.org/10.1029/96JC02775.
Menemenlis, D., Fukumori, I., Lee, T., 2005a. Using Green′s functions to calibrate an Ocean General Circulation model. Monthly Weather Review 133, 1224–1240 http://dx.doi.org/10.1175/MWR2912.1.
Menemenlis, D., Hill, C., Adcroft, A., Campin, J.M., Cheng, B., Ciotti, B., Fukumori, I., Koehl, A., Heimbach, P., Henze, C., Lee, T., Stammer, D., Taft, J., Zhang, J., 2005b. NASA supercomputer improves prospects for ocean climate research. EOS, Transactions, American Geophysical Union 86, 89.
Mork, K.A., Skagseth, Ø., 2005. Annual sea surface height variability in the Nordic seas. In: Drange, H., et al. (Eds.), The Nordic Seas: An Integrated Perspective Oceanography, Climatology, Biogeochemistry, and Modeling, Geophys. Monogr. Ser, vol. 158. AGU, Washington, D. C., pp. 51–64 http://dx.doi.org/10.1029/158GM05.
Proshutinsky, A., Ashik, I., Häkkinen, S., Hunke, E., Krishfield, R., Maltrud, M., Maslowski, W., Zhang, J., 2007. Sea level variability in the Arctic Ocean from AOMIP models. Journal of Geophysical Research 112, C04S08, http://dx.doi.org/10.1029/2006JC003916.
Proshutinsky, A., Ashik, I.M., Dvorkin, E.N., Hakkinen, S., Krishfield, R.A., Peltier, W.R., 2004. Secular sea level change in the Russian sector of the Arctic Ocean. Journal of Geophysical Research 109, C03042, http://dx.doi.org/10.1029/2003JC002007.
Richter, K., Nilsen, J.E. Ø., Drange, H., 2012. Contributions to sea level variability along the Norwegian coast for 1960–2010. Journal of Geophysical Research 117, C05038, http://dx.doi.org/10.1029/2011JC007826.
Skagseth, Ø., Furevik, T., Ingvaldsen, R., Loeng, H., Mork, K.A., Orvik, K.A., Ozhigin, V., 2008. Volume and heat transports to the Arctic Ocean via the Norwegian and Barents seas. In: Dickson, R.R., Meincke, J., Rhines, P. (Eds.), Arctic-Subarctic Ocean Fluxes. Springer, Dordrecht, pp. 45–64.
Steele, M., Ermold, W., 2007. Steric sea level change in the Northern seas. Journal of Climate 20, 403–417.
Terziev, F.S., G.V. Girduk, G.G. Zhukova, S.L. Dzhenyuk, (Eds.), 1990. Hydrometeorology and hydrochemistry of the seas of the USSR, vol. 1, Barents Sea, Issue 1, Hydrometeorological Conditions, Hydrometeoizdat, Leningrad (in Russia).
Thomas, M., 2002: Ocean Induced Variations of Earth′s Rotation—Results from a Simultaneous Model of Global Ocean Circulation and Tides. Ph.D. Dissertation. University of Hamburg, Germany, 129 pp.
Volkov, D.L., Larnicol, G., Dorandeu, J., 2007. Improving the quality of satellite altimetry data over continental shelves. Journal of Geophysical Research 112, C06020, http://dx.doi.org/10.1029/2006JC003765.
Volkov, D.L., Pujol, M.-I., 2012. Quality assessment of a satellite altimetry data product in the Nordic, Barents, and Kara seas. Journal of Geophysical Research 117, C03025, http://dx.doi.org/10.1029/2011JC007557.
Volkov, D.L., Belonenko, T.V., Foux, V.R., 2013. Puzzling over the dynamics of the Lofoten Basin—a sub-Arctic hot spot of ocean variability. Geophysical Research Letters, 40, http://dx.doi.org/10.1002/grl.50126.
Wahr, J., Swenson, S., Velicogna, I., 2006. Accuracy of GRACE mass estimates. Geophysical Research Letters 33, L06401, http://dx.doi.org/10.1029/2005GL025305.